Volume 51
Number 17
7 May 2022
Pages 6489-6980

Dalton Transactions

An international journal of inorganic chemistry

rsc.li/dalton

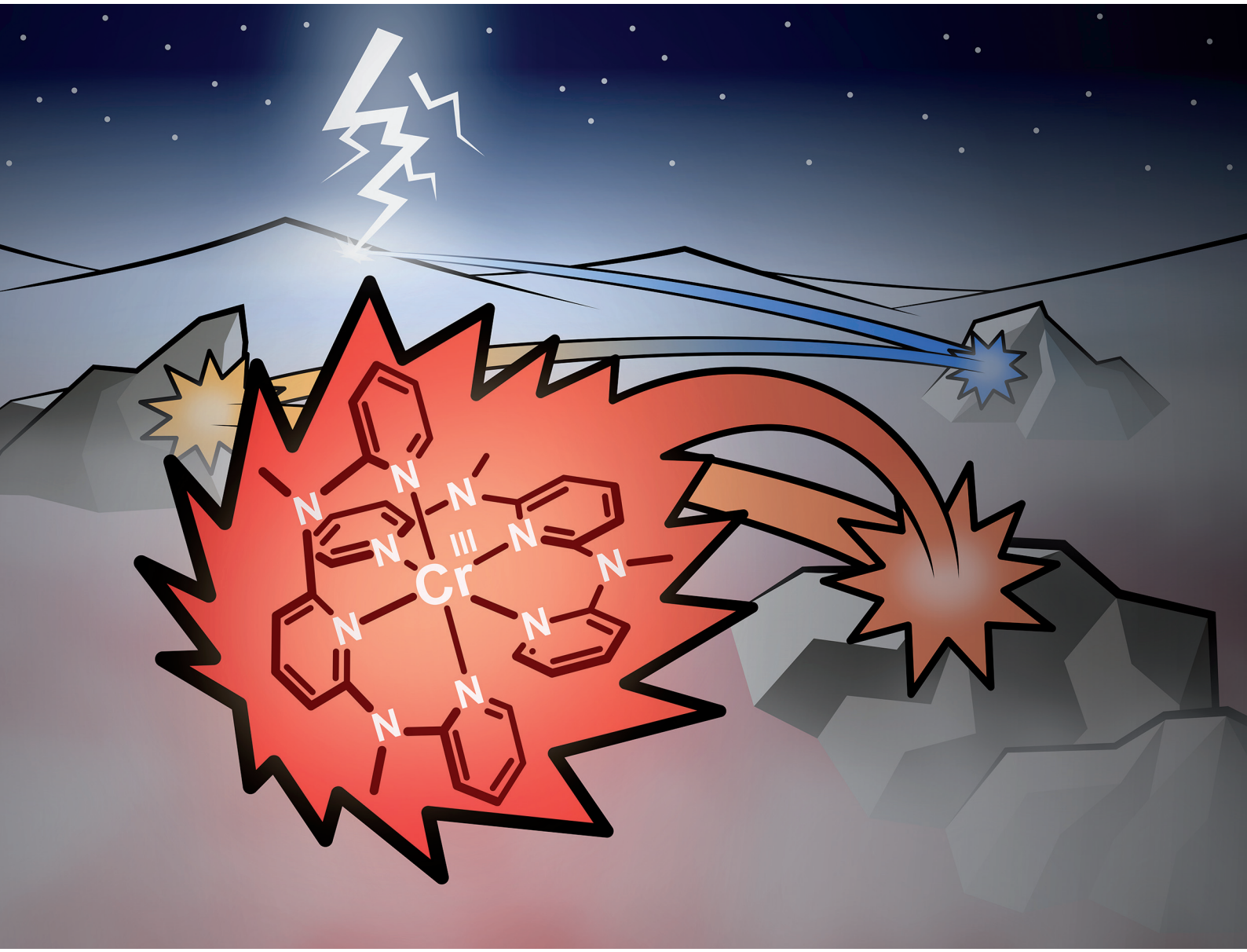

ISSN 1477-9226

ROYAL SOCIETY OF CHEMISTRY

FRONTIER
Katja Heinze *et al.*
Molecular ruby: exploring the excited state landscape

Dalton Transactions

ROYAL SOCIETY OF CHEMISTRY

FRONTIER

View Article Online
View Journal | View Issue

Check for updates

Cite this: *Dalton Trans.*, 2022, **51**, 6519

Molecular ruby: exploring the excited state landscape†

Winald Robert Kitzmann, [a] Charusheela Ramanan, [b,c] Robert Naumann [a] and Katja Heinze *[a]

Received 22nd February 2022,
Accepted 5th April 2022

DOI: 10.1039/d2dt00569g

rsc.li/dalton

The discovery of the highly NIR-luminescent molecular ruby $[Cr(ddpd)_2]^{3+}$ (ddpd = *N*,*N*′-dimethyl-*N*,*N*′-dipyridin-2-ylpyridine-2,6-diamine) has been a milestone in the development of earth-abundant luminophors and has led to important new impulses in the field of spin–flip emitters. Its favourable optical properties such as a high photoluminescence quantum yield and long excited state lifetime are traced back to a remarkable excited state landscape which has been investigated in great detail. This article summarises the results of these studies with the aim to create a coherent picture of the excited state ordering and the ultrafast as well as long-timescale dynamics. Additional experimental data is provided to fill in gaps left by previous reports.

Introduction

In metal-to-ligand charge transfer (MLCT) emitters such as $[Ru(bpy)_3]^{2+}$ an excited state ordering of ^{1}GS, ^{3}MLCT, ^{1}MLCT and ^{3}MC is commonly found and exploited for different applications like photocatalysis (GS = ground state, MC = metal-centered state, bpy = 2,2′-bipyridine).[1]

In contrast, spin–flip emitters with the prototype ruby ($Al_2O_3:Cr^{3+}$) possess a richer excited state landscape in the relevant energy region.[2,3] For a d^3 electron configuration in O_h symmetry as found in octahedral Cr^{III} compounds, the metal-centered $^4A_2$, $^2E/^2T_1$, $^2T_2$ and $^4T_2$ states are important (Fig. 1). Additionally, charge transfer states can play a role in excitation and decay processes.[4,5]

In d^3 spin–flip emitters, excitation to the $^4T_2$ state is followed by intersystem crossing (ISC) to the doublet states $^2E/^2T_1$, from which phosphorescence to the quartet GS $^4A_2$ occurs.[6] As the term "spin–flip emitter" suggests, this transition merely involves the flipping of a single electron spin. The ^2E state features only unpaired electrons, while two electrons are paired in $^2T_1$ and $^2T_2$ states (Fig. 1).[4] For spin–flip emission, the $^2E/^2T_1$ states need to be the lowest excited states. Additionally, a large energy gap to the $^4T_2$ state is necessary to prevent $^2E/^2T_1 \rightarrow {}^4T_2$ back-ISC (bISC) and fast relaxation *via* $^4T_2 \rightarrow {}^4A_2$ fluorescence, internal conversion (IC) or ligand dissociation.[7] This is achieved *via* a large ligand field splitting Δ_O, since the energy of the interconfigurational $^4T_2$ state is linearly dependent on Δ_O, while the energies of the intraconfigurational states ^2E, $^2T_1$ and $^2T_2$ are essentially independent of Δ_O and instead vary with interelectronic repulsion quantified by the Racah parameters *B* and *C* (Fig. 1).[8] In general, Cr^{III} ions possess a small instrinsic ligand field splitting due to the primogenic effect.[9]

In ruby, the six oxido ligands exert a strong ligand field on the Cr^{3+} ions because of the short Cr–O distance imposed by the corundum host lattice. This results in a $^4T_2$ absorption

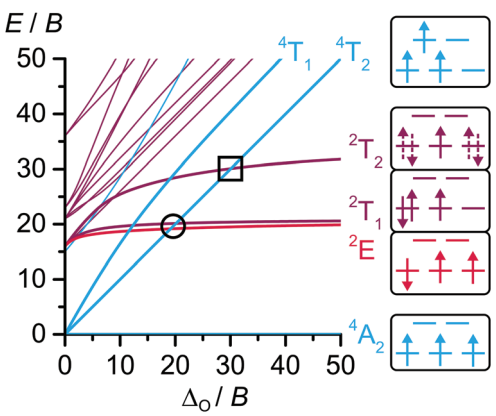

Fig. 1 Tanabe–Sugano (TS) diagram of the d^3 electron configuration in an octahedral ligand field with C/B = 4 and exemplary microstates.[4,14] The two important excited state quartet/doublet crossing points are highlighted with a circle and a square, respectively. Dotted lines in the microstates indicate strong electronic mixing.

[a]*Department of Chemistry, Johannes Gutenberg University of Mainz, Mainz, Germany. E-mail: katja.heinze@uni-mainz.de*
[b]*Department of Physics and Astronomy, Vrije Universiteit Amsterdam, Amsterdam, Netherlands*
[c]*Max-Planck-Institute for Polymer Research, Mainz, Germany*

† Electronic supplementary information (ESI) available. See DOI: https://doi.org/10.1039/d2dt00569g

band at 551 nm and strong phosphorescence at 694.3 (R_1 line) as well as 692.9 nm (R_2 line) *via* the slightly split $^2E \rightarrow {}^4A_2$ transitions.[2,10] This emission with a lifetime of 4268 ± 6 μs and a photoluminescence quantum yield of 90 ± 5% was the cornerstone of the first laser in 1960.[2,3,11] In contrast, molecular Cr^{III} complexes like $[Cr(bpy)_3]^{3+}$ (Φ = 0.089%)[12] or $[Cr(tpy)_2]^{3+}$ (Φ < 0.001%)[13] suffer from poor quantum yields due to the small Δ_0 facilitating bISC and other deactivation pathways (tpy = 2,2′:6′,2″-terpyridine).[4]

Ground and excited states of the molecular ruby

In 2015, a breakthrough was achieved with the discovery of the strongly near infrared (NIR) luminescent complex $[Cr(ddpd)_2]^{3+}$ (Fig. 2, ddpd = *N*,*N*′-dimethyl-*N*,*N*′-dipyridin-2-ylpyridine-2,6-diamine). Irradiation in the $^4A_2 \rightarrow {}^4T_2$ and ligand-to-metal charge transfer (LMCT) absorption band at 435 nm yields a very intense dual phosphorescence at 738 and 775 nm ($^2T_1/^2E \rightarrow {}^4A_2$, purple area in Fig. 3) with a lifetime of 1122 μs and quantum yields of 11% in aqueous and 13.7% in acetonitrile solution at room temperature.[7,15] The excitation spectra observed at 775 nm closely follow the absorption spectra in the region 300–500 nm demonstrating that all states efficiently evolve to the emissive states. Indeed, only a weak fluorescence ($^4T_2 \rightarrow {}^4A_2$, blue area in Fig. 3) at 500 nm was found with a lifetime[7] of 3 ns and a quantum yield of approximately 0.01% (see ESI†). Overall, $[Cr(ddpd)_2]^{3+}$ vastly outperforms classical chromium(III) complexes and hence was called molecular ruby.[16] Detailed follow-up studies revealed several aspects underlying the reasons for its success.

The $^4A_2$ GS of $[Cr(ddpd)_2]^{3+}$ exhibits an almost spherical spin distribution as expected for a d^3 configuration (Fig. 4). A small zero-field splitting of D = +0.18 cm^{-1} and E = −0.06 cm^{-1} was found through Q-band electron paramagnetic resonance (EPR) spectroscopy at 5 K.[17] The $[CrN_6]$ σ-skeleton is close to octahedral, but the π-bonding lowers the actual symmetry (point group D_2). Thus, all E and T terms found in the TS diagram (Fig. 1) should be split in $[Cr(ddpd)_2]^{3+}$.

How large is the ligand field splitting Δ_0 in $[Cr(ddpd)_2]^{3+}$, in other words, where is $[Cr(ddpd)_2]^{3+}$ located in the TS diagram (Fig. 1)? Investigation of the absorption bands including the

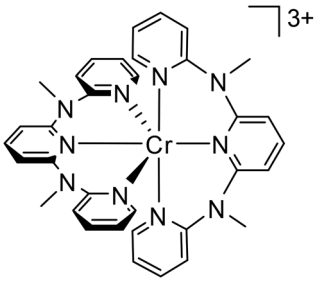

Fig. 2 Molecular structure of $[Cr(ddpd)_2]^{3+}$.

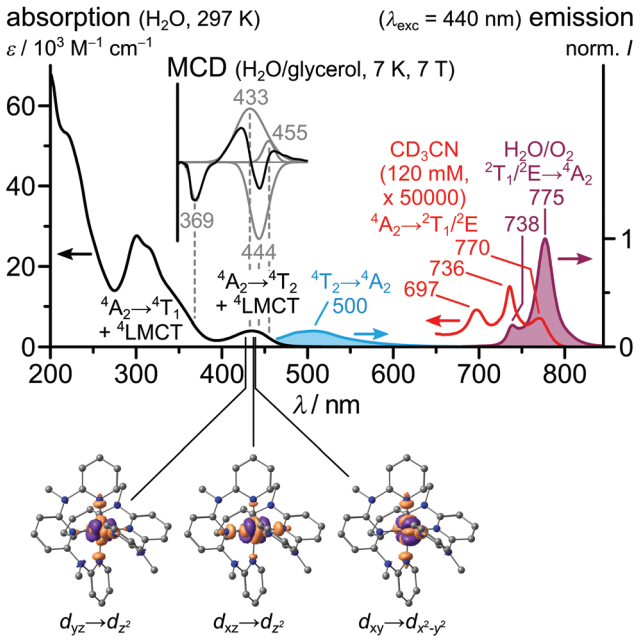

Fig. 3 Absorption spectra (H_2O: black line, CD_3CN: red line, see ESI†), MCD spectrum (H_2O/glycerol, 7 K, 7 T) and separately normalized fluorescence (blue area) and phosphorescence spectra (purple area, aerated H_2O) of $[Cr(ddpd)_2]^{3+}$ and TD-DFT (B3LYP/Def2-TZVPP) calculated difference densities of the $^4A_2 \rightarrow {}^4T_2$ transitions with an isosurface value of 0.005 a.u.[7,17]

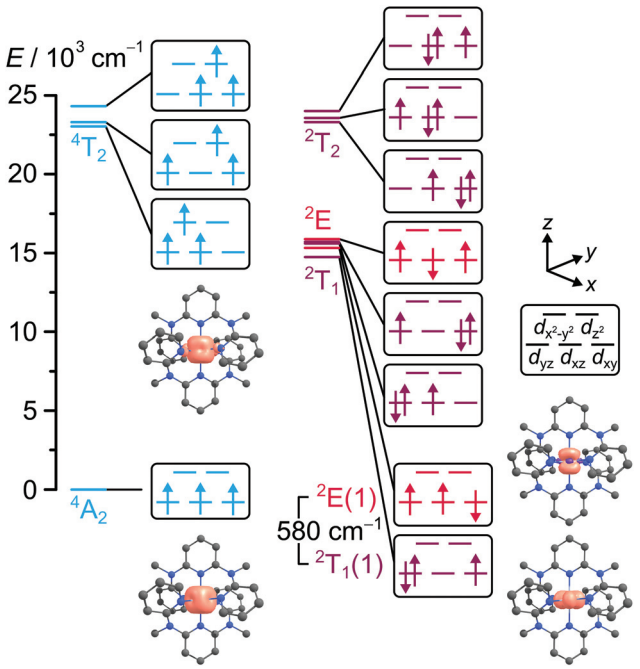

Fig. 4 CASSCF(7,12)-NEVPT2 derived state diagram at the GS geometry of $[Cr(ddpd)_2]^{3+}$ with dominating electron configurations in the microstates and calculated spin-densities at an isosurface value of 0.05 a.u.[20]

$^4A_2 \rightarrow {}^4T_2$ transition at 435 nm with magnetic circular dichroism (MCD) spectroscopy at 7 K and 7 T in frozen solution and DFT calculations revealed $\Delta_0 \gg 20\ B$ (Fig. 3).[17] Thus, the large

$^4T_2$–$^2T_1$/^2E energy gap effectively suppresses bISC to the $^4T_2$ states as relaxation pathway. The large Δ_0 was rationalized with the strongly σ-donating nature of the electron-rich ligand ddpd and its six-membered chelate rings leading to an almost perfectly octahedral [CrN_6] coordination geometry and a large metal–ligand σ-orbital overlap.[7]

Multireference calculations with perturbation correction and *ab initio* ligand field analysis (CASSCF(3,5)-NEVPT2-AILFT) yielded Δ_0 = 23 000 cm^{-1}, B = 964 cm^{-1} and C/B = 3.08 as ligand field parameters (B(free Cr^{3+} ion) = 918 cm^{-1})[18] and split E and T states.[19] A larger active space in a CASSCF(7,12)-NEVPT2 calculation was used to generate the state diagram in Fig. 4.[20] According to this calculation, Δ_0 of $[Cr(ddpd)_2]^{3+}$ is located close to the second quartet-doublet crossing point $^4T_2$–$^2T_2$ in the TS diagram (black square in Fig. 1). Although the absolute calculated values are too high, trends can be well reproduced.[19] In contrast to perfectly octahedral complexes such as $[Cr(CN)_6]^{3-}$, CASSCF(7,12)-NEVPT2 calculations of $[Cr(ddpd)_2]^{3+}$ place a spin-paired $^2T_1$-derived microstate below a ^2E-derived true spin–flip microstate ($^2T_1$(1) and ^2E(1) in Fig. 4).[19,20] Thus the energy level ordering calculated for $[Cr(ddpd)_2]^{3+}$ (Fig. 4) differs from the TS diagram (Fig. 1).

The sharp phosphorescence bands (purple area in Fig. 3) suggest that the emissive excited doublet states $^2T_1$(1) and ^2E(1) are essentially nested, *i.e.* only weakly distorted relative to the $^4A_2$ GS, as expected for the unchanged $(t_{2g})^3$ electron configuration in the doublet states compared to the GS (Fig. 4).

The CASSCF calculated energy difference between the lowest doublet states ΔE amounts to 580 cm^{-1}.[20] Experimentally, values of 650 cm^{-1} and 700 cm^{-1} were derived from the emission band energy difference and the slopes of Boltzmann plots obtained from temperature dependent emission spectra in various solvents (Fig. 5), respectively.[21]

The ^2E(1) and $^2T_1$(1) states share the same lifetime as well as a similar geometry as the $^4A_2$ ground state suggesting only a very small barrier for internal conversion (IC) between the two lowest doublet states. The two lowest emissive states are in thermal equilibrium (Fig. 5).[21] Using ΔE = 700 cm^{-1} a Boltzmann factor N_{738}/N_{775} of 0.032 is calculated at 293 K.

The area ratio A_{740}/A_{776} of the emission bands in MeCN fitted with two Voigt functions amounts to 0.091 (see ESI, Fig. S2 and Table S2†) indicating that the radiative transition $^2E(1) \rightarrow {}^4A_2$ at 738 nm is approximately 0.091/0.032 = 2.8 times more allowed than the $^2T_1(1) \rightarrow {}^4A_2$ radiative transition at 775 nm. The spin-forbidden $^4A_2 \rightarrow {}^2T_1/{}^2E$ absorption bands (red line in Fig. 3) with extinction coefficients of <0.3 M^{-1} cm^{-1} in a concentrated acetonitrile solution were fitted with three Voigt functions and give a similar area ratio of A_{736}/A_{770} = 2.96 (see ESI, Fig. S1 and Table S1†). This also indicates that the $^4A_2 \rightarrow {}^2E(1)$ transition is *ca.* 3 times more allowed than the $^4A_2 \rightarrow {}^2T_1(1)$ transition. Based on the calculations presented in Fig. 4 these bands were assigned to $^4A_2 \rightarrow {}^2T_1(1)$, $^4A_2 \rightarrow {}^2E(1)$ and $^4A_2 \rightarrow {}^2T_1(2)$ transitions, respectively (see ESI, Table S1† for details). The area ratio of the 736 and 770 nm absorption bands of 3.0 agrees with the value derived from the emission data (see above). The small Stokes shifts of 37 and 83 cm^{-1} for the high-energy and low-energy emission bands, respectively, support the proposed nested nature of the doublet excited states. The data also suggest a slightly more pronounced geometric distortion of the $^2T_1$ state compared to the ^2E state, which may facilitate the radiative transitions between the GS and ^2E(1) state.

Below *ca.* 130 K (KBr pellet), the high-energy emission band vanishes and only the lowest $^2T_1$ derived microstate is populated (Fig. 6). Furthermore, the $^2T_1(1) \rightarrow {}^4A_2$ emission band shows vibrational progression at 795 and 811 nm (Fig. 6).[22] The doublet state population $^2E(1)/{}^2T_1(1)$ was modulated in Fourier-transform infrared (FTIR) pump–pump–probe(IR) and pump–dump–probe(IR) experiments at 290 and 20 K.[22] Step-scan FTIR spectroscopy differentiated ^2E and $^2T_1$ derived microstates and suggested that $[Cr(ddpd)_2]^{3+}$ in the ^2E(1) state nearly perfectly resembles the $^4A_2$ geometry, while the $^2T_1(1)$ derived microstate is slightly distorted giving rise to an excited

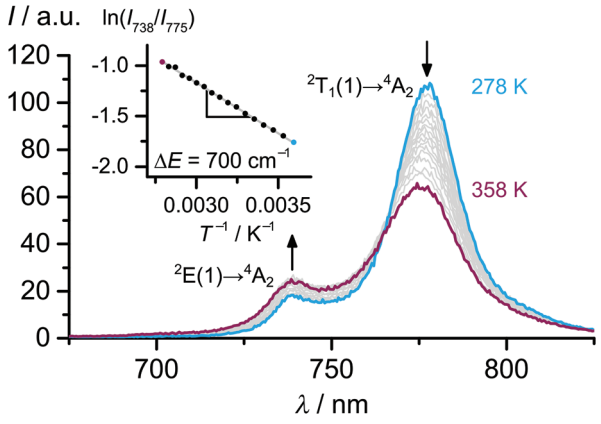

Fig. 5 Phosphorescence spectra of $[Cr(ddpd)_2][BF_4]_3$ in H_2O at variable temperature. The inset shows the Boltzmann plot $\ln(I_{738}/I_{775})$ *vs.* T^{-1}/K^{-1}. The slope corresponds to $-\Delta E/k_B$ with the energy difference of the emissive states ΔE and the Boltzmann constant k_B.[21]

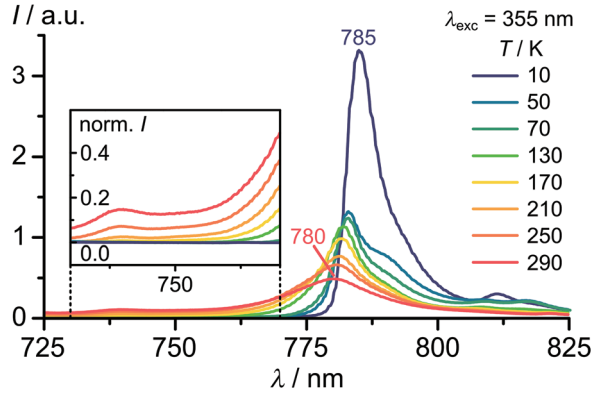

Fig. 6 Phosphorescence spectra of $[Cr(ddpd)_2][BF_4]_3$ as KBr pellet between 290 and 10 K after excitation at 355 nm. The inset shows the region of the transition at about 739 nm, where the low-energy emission intensity at each temperature is normalized to 1 for better visibility of the decrease of the high-energy band at lower temperature.[22]

state IR spectrum which differs from the GS IR spectrum.[22] These experiments show the effect of pairing two electrons in a t_{2g}-orbital. However, the exact (Jahn–Teller) distortional mode is not fully elucidated, yet.

Pressure shifts both emissive doublet states to lower energies similar to ruby (−0.8 cm^{-1} $kbar^{-1}$)[23] but with a much stronger effect, *i.e.* 13–15 cm^{-1} $kbar^{-1}$ for the low-energy $^2T_1(1)$ and *ca.* 8 cm^{-1} $kbar^{-1}$ for the high-energy $^2E(1)$ emission (Fig. 7).[20] These energy shifts result from small geometric changes under pressure likely involving N–Cr–N angles which is much more pronounced in the molecular ruby than in the oxidic lattice of ruby.[20]

Ultrafast dynamics and dark excited states

According to CASSCF-NEVPT2 calculations, the $^4T_2$ states are approximately degenerate with the higher-energy $^2T_2$ states at the Franck Condon (FC) geometry (Fig. 4). This implies, that Δ_0 of $[Cr(ddpd)_2]^{3+}$ is well-separated from the first excited state crossing point $^2T_1/^2E/^4T_2$ (black circle in Fig. 1) but very close to the second crossing point $^2T_2/^4T_2$ in the TS diagram (in the FC state at GS geometry, black square in Fig. 1). Consequently, when exciting $[Cr(ddpd)_2]^{3+}$ to the $^4T_2$ states, a high density of $^2T_2$ states with their vibrational levels is present in this FC region. Additionally, the CASSCF calculations yielded significant spin–orbit couplings (SOCs) of 42, 97 and 45 cm^{-1} for the pathways from $^4T_2(1)$ to $^2T_2(2)$, $^2E(1)$ and $^2T_1(2)$, respectively.[19] This is in agreement with El-Sayed's rule that states that SOC between two states is large when a change in multiplicity (here: quartet → doublet) is accompanied by a change in orbital angular momentum (here: $e_g^* \rightarrow t_{2g}$).[24] Overall, the high density of states, relatively large SOC and small $^4T_2$–$^2T_2$ energy difference at FC geometry could facilitate $^4T_2 \rightarrow {}^2T_2$ ISC in $[Cr(ddpd)_2]^{3+}$.[25]

In fact, the fully relaxed, emissive doublet states $^2T_1/^2E$ of $[Cr(ddpd)_2]^{3+}$ are reached within τ = 3.5 ps after excitation to $^4T_2$ states.[26] Very likely, the ISC process is even faster (τ_{ISC} < 200 fs) and the picosecond time constant rather applies to vibrational cooling (VC) and IC between doublet states. The fluorescence quantum yield $\Phi_{Fl} \approx 0.01\%$ allows to derive an upper limit for the ISC quantum yield of $\Phi_{ISC} < 99.99\%$. In the structurally similar $[Cr(bpmp)_2]^{3+}$ (bpmp = 2,6-bis(2-pyridylmethyl)pyridine) a lower limit for Φ_{ISC} of 92 ± 5% was determined *via* doublet–triplet energy transfer and laser flash photolysis experiments.[19]

Interestingly, in the classical organic sensitizer benzophenone $Ph_2C{=}O$ the predicted relaxation cascade $S_1 \rightarrow T_2 \rightarrow T_1 \rightarrow S_0$ with almost isoenergetic T_2 and S_1 states[27] is analogous to the one proposed for $[Cr(ddpd)_2]^{3+}$ with $^4T_2 \rightarrow {}^2T_2 \rightarrow {}^2T_1/{}^2E \rightarrow {}^4A_2$.

Femtosecond transient absorption spectra covering the Vis-NIR range after excitation with 435 nm pulses show broad excited state absorptions (ESA) covering the 500–900 nm spectral range (ESA1: 14 000 cm^{-1} and ESA2: 12 300 cm^{-1}, Fig. 8). These evolve with a common time constant of *ca.* 3.2 ps to ESAs at 534 nm (ESA3: 18 700 cm^{-1}) and 1389 nm (ESA4: 7200 cm^{-1}, see ESI, Fig. S4 and S5†).[26] ESA3 and ESA4 are assigned to $^2T_1/^2E \rightarrow {}^2$LMCT and $^2T_1/^2E \rightarrow {}^2T_2$ transitions, respectively. Addition of ESA3 to the $^2T_1$ energy yields an energy of 31 600 cm^{-1} (316 nm) for the ^{2}LMCT state, which corresponds to the respective ^{4}LMCT absorptions found in the GS absorption spectra (Fig. 3). ESA4 in the NIR region helps to experimentally estimate the energy of the dark $^2T_2$ states by summation of the emission energy (775 nm, 12 900 cm^{-1}) and the ESA4 energy (1389 nm, 7200 cm^{-1}) giving 20 100 cm^{-1} (498 nm). This energy is indeed slightly below the CASSCF calculated energy of $^4T_2$ states at the GS geometry.

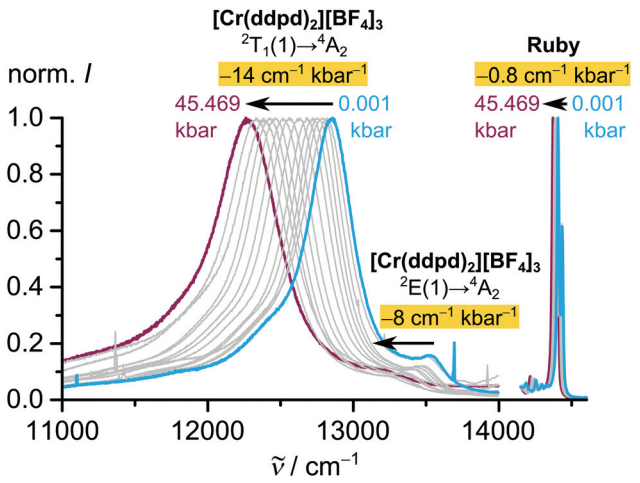

Fig. 7 Normalized pressure-dependent phosphorescence spectra of $[Cr(ddpd)_2][BF_4]_3$ between 0.001 and 45.469 kbar in nujol together with a ruby crystal (right).[20,23]

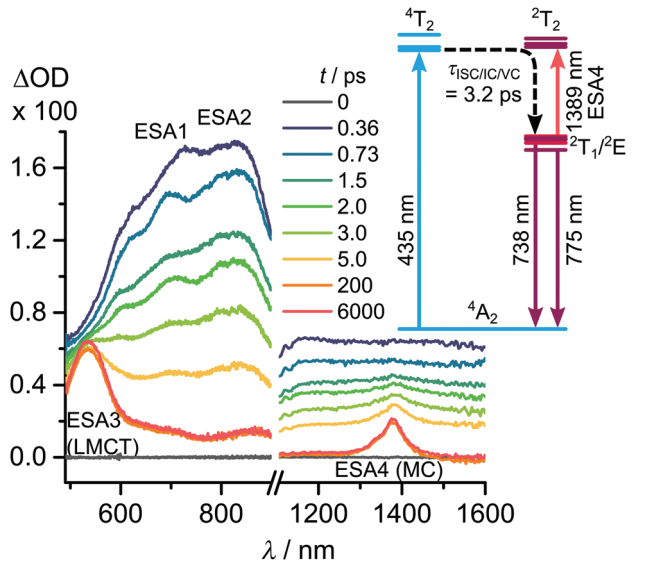

Fig. 8 Fs-Transient absorption spectra of $[Cr(ddpd)_2]^{3+}$ in CH_3CN after excitation at 435 nm and excited state diagram with CASSCF(7,12)-NEVPT2 calculated energies (see ESI† for details, ESA = excited state absorption).[26]

The $^4T_2$ states should be Jahn–Teller distorted due to the singly occupied e_g^* orbitals and the doubly occupied t_{2g} orbitals. Indeed DFT calculations reveal, that the optimised lowest $^4T_2$ microstate displays elongated Cr–N bond lengths of terminal pyridines in a single ddpd ligand (2.08 Å → 2.42 Å).[7] As the energy of this quartet state drops dramatically with increasing Cr–N distances, it is essential for high stability and strong emission that the ISC is fast and preferably in the FC region before vibrational relaxation in the $^4T_2$ state takes place.

With this interpretation, $[Cr(ddpd)_2]^{3+}$ hits a sweet spot in the TS diagram which enables a fast ISC pathway $^4T_2(1) \rightarrow {}^2T_2(2)$ to the doublet states at the FC geometry *via* the dark $^2T_2$ states in addition to the direct $^4T_2(1) \rightarrow {}^2E(1)$ and $^4T_2(1) \rightarrow {}^2T_1(2)$ pathways with a higher energy difference. The vibrational relaxation within the quartet states along the Cr–N Jahn–Teller modes (in *x*- and *y*-direction)[28] might be comparably slow due to a low potential energy gradient at the FC geometry. In any case, the fast ISC avoids vibrational relaxation within the quartet states and thus suppresses undesired fluorescence from the $^4T_2$ state, non-radiative decay by $^4T_2$ surface crossing with the GS, and even Cr–N bond dissociation. In fact, $[Cr(ddpd)_2]^{3+}$ is particularly photostable, even at low pH in contrast to *e.g.* $[Cr(bpy)_3]^{3+}$.[6,7]

Long-lived spin–flip states

The dynamics of the long-lived excited states depend on the presence of high-energy oscillators[29] and quenchers,[26,30] the excited state distortion[22] and the temperature.[21,22]

The doublet states can relax non-radiatively *via* energy transfer (EnT) to vibrational overtones of nearby C–H oscillators (multiphonon relaxation).[31] $[Cr(ddpd)_2]^{3+}$ has a comparably small spectral overlap integral (SOI) with the ν^4 and the ν^5 C–H overtones associated with the pyridine rings (Fig. 9). This results in a small rate constant for non-radiative decay k_{nr} and thus a high quantum yield.[29]

After deuteration of the ligand, there is only a significant SOI with a higher C–D overtone (ν^6) with an extinction coefficient which is roughly two orders of magnitude smaller than ν^5(C–H).[29] Thus, deuterated $[Cr(ddpd)_2]^{3+}$ shows an even smaller k_{nr} and a record quantum yield of 30%. The limited increase from 13.7 to 30% might in part be associated with the near degeneracy of the fifth C–D overtone (ν^6) and the $^2T_1(1) \rightarrow {}^4A_2$ emission band (Fig. 9),[29] yet direct $^2T_1 \rightarrow {}^4A_2$ ISC plays a role as well, irrespective of the deuteration level.

As stated above, at high enough thermal energy the ^2E and $^2T_1$ states equilibrate leading to dual emission. Below *ca.* 130 K, the $^2E(1)$ band vanishes, the $^2T_1(1)$ emission band sharpens and shifts to lower energy (785 nm in KBr, Fig. 6) showing that the $^2T_1(1)$ state is stabilized (vertical displacement of the $^2T_1(1)$ potential energy well). The phosphorescence quantum yield increases dramatically between 70 and 10 K (Fig. 6).[22]

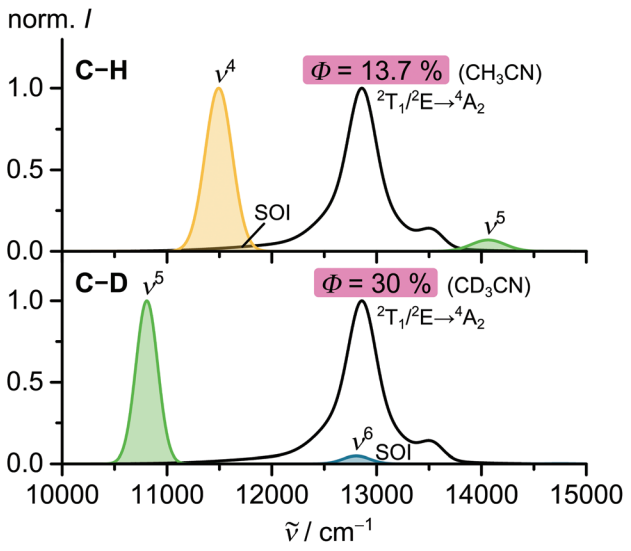

Fig. 9 C–H and C–D vibrational overtone spectra of model pyridine ligands and their overlap with the phosphorescence bands of $[Cr(ddpd)_2]^{3+}$ (SOI = spectral overlap integral).[29]

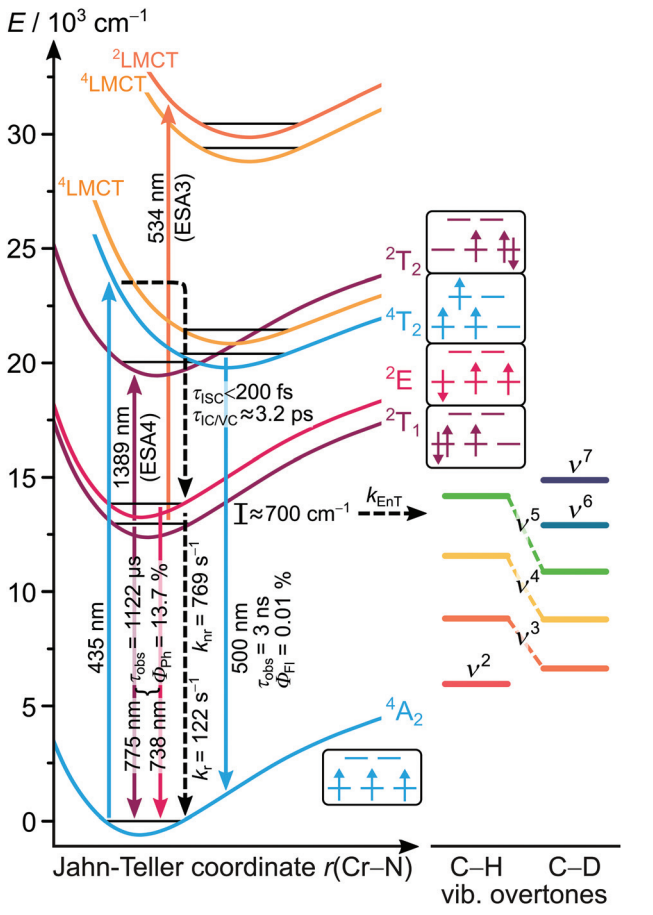

Fig. 10 Experimentally[7,21,26,29] determined excited state energy landscape of the molecular ruby $[Cr(ddpd)_2]^{3+}$ in CH_3CN and time constants determined so far with exemplary microstates for the MC states derived from CASSCF(7,12)-NEVPT calculations,[20] the rate constant of non-radiative decay k_{nr} and the rate constant for energy transfer to vibrational overtones k_{EnT} (which is included in k_{nr}). The Jahn–Teller coordinate refers to the $^4T_2$ state while the $^{4/2}$LMCT states likely display other distortions from the GS geometry.

The increase in phosphorescence quantum yield at very low temperatures might be associated with the sharpening of the $^2T_1(1)$ emission band, which reduces the SOI with the third C–H vibrational overtone (ν^4) of the ligand. Additional explanations for the higher phosphorescence quantum yield at low T might be a reduction of other thermally activated non-radiative decay pathways and the enhancement of the radiative decay *via* larger distortion of the $^2T_1(1)$ state relative to the ground state lifting Laporte's rule.[32] In fact, the radiative rate k_r decreases dramatically from pseudooctahedral $[Cr(ddpd)_2]^{3+}$ ($k_r = \Phi/\tau = 122\ s^{-1}$ in CH_3CN)[15] to the electronically similar but perfectly centrosymmetric Cr^{III} complex $[Cr(tpe)_2]^{3+}$ ($k_r = 18.2\ s^{-1}$, tpe = 1,1,1-tris(pyrid-2-yl)ethane).[33]

Triplet oxygen quenches the long-lived phosphorescence of $[Cr(ddpd)_2]^{3+}$ induced by 435 nm excitation *via* Dexter energy transfer to form the ground state complex and $^1O_2$ with a quantum yield of 61% in acetonitrile.[26] The typical $^1O_2$ phosphorescence at 1274 nm appears even after direct spin-forbidden excitation of $[Cr(ddpd)_2]^{3+}$ to its $^2T_1/^2E$ states at 771 and 735 nm, respectively (see ESI, Fig. S3†), confirming that the doublet states of $[Cr(ddpd)_2]^{3+}$ sensitize $^1O_2$.

The excited state landscape of $[Cr(ddpd)_2]^{3+}$ is sketched in Fig. 10 along with experimentally determined energies, rate constants and quantum yields, summarising excitation, excited state dynamics to the emissive doublet states, excited state absorptions, non-radiative relaxation in particular multi-phonon relaxation as well as radiative transitions.

Future outlook

Following the report of $[Cr(ddpd)_2]^{3+}$ the underlying design principles gave rise to a large number of highly luminescent Cr^{III} complexes.[19,33–35,36] Current efforts are directed to shifting the emission energy of molecular ruby derivatives to lower or higher energy by ligand modifications[19,37] and by modification of the central metal and electron configuration from d^3-Cr^{III} to d^2-V^{III}.[38] Variation of the counter ions of $[Cr(ddpd)_2]^{3+}$ and surrounding matrix as well as shielding of the metal center by sterically demanding groups proved to be fruitful strategies to enhance quantum yields and lower oxygen sensitivity.[15] Applications of molecular ruby derivatives in upconversion,[39] circularly polarized emission,[34,35,40] sensing,[20,21,41] photosensitization for organic synthesis[26] or photodynamic therapy[30] and others had already been demonstrated or are currently explored.

Author contributions

W. R. K. provided the resources (synthesis of $[Cr(ddpd)_2]^{3+}$), performed the investigation (measurement of Φ_{Fl}), visualized the data and wrote the original drafts. C. R. performed the fs-transient absorption spectroscopy. R. N. performed the investigation of the phosphorescence lifetimes, the spin-forbidden absorption and $^1O_2$ sensitization experiments with NIR excitation. K. H. conceptualized the article, acquired the funding, supervised the project and wrote the original drafts.

Conflicts of interest

There are no conflicts to declare.

Acknowledgements

The authors thank Dr Johannes Hunger for his support in this project and Dr Christoph Förster for constructive criticism of the manuscript. Financial support from the Deutsche Forschungsgemeinschaft [DFG, Priority Program SPP 2102 "Light-controlled reactivity of metal complexes" (HE 2778/13-1)] is gratefully acknowledged. We thank the DFG for grant INST 247/1018-1 FUGG to K. H.; W. R. K. is grateful for a Kekulé scholarship of the Fonds der Chemischen Industrie.

Notes and references

1 (*a*) F. Teplý, *Phys. Sci. Rev.*, 2020, **5**, 20170171; (*b*) O. S. Wenger, *Chem. – Eur. J.*, 2019, **25**, 6043–6052.
2 T. H. Maiman, *Nature*, 1960, **187**, 493–494.
3 C. Degli Esposti and L. Bizzocchi, *J. Chem. Educ.*, 2007, **84**, 1316.
4 W. R. Kitzmann, J. Moll and K. Heinze, *Photochem. Photobiol. Sci.*, 2022, DOI: **10.1007/s43630-022-00186-3**, in press.
5 R. D. Dill, R. I. Portillo, S. G. Shepard, M. P. Shores, A. K. Rappé and N. H. Damrauer, *Inorg. Chem.*, 2020, **59**, 14706–14715.
6 S. Otto, M. Dorn, C. Förster, M. Bauer, M. Seitz and K. Heinze, *Coord. Chem. Rev.*, 2018, **359**, 102–111.
7 S. Otto, M. Grabolle, C. Förster, C. Kreitner, U. Resch-Genger and K. Heinze, *Angew. Chem., Int. Ed.*, 2015, **54**, 11572–11576.
8 D. Zare, B. Doistau, H. Nozary, C. Besnard, L. Guénée, Y. Suffren, A.-L. Pelé, A. Hauser and C. Piguet, *Dalton Trans.*, 2017, **46**, 8992–9009.
9 (*a*) Y. Tang, S. Zhao, B. Long, J.-C. Liu and J. Li, *J. Phys. Chem. C*, 2016, **120**, 17514–17526; (*b*) J. K. McCusker, *Science*, 2019, **363**, 484–488.
10 D. D. Ragan, R. Gustavsen and D. Schiferl, *J. Appl. Phys.*, 1992, **72**, 5539–5544.
11 R. S. Quimby and W. M. Yen, *J. Appl. Phys.*, 1980, **51**, 1780–1782.
12 A. D. Kirk and G. B. Porter, *J. Phys. Chem.*, 1980, **84**, 887–891.
13 J.-R. Jiménez, B. Doistau, C. Besnard and C. Piguet, *Chem. Commun.*, 2018, **54**, 13228–13231.
14 (*a*) Y. Tanabe and S. Sugano, *J. Phys. Soc. Jpn.*, 1954, **9**, 753–766; (*b*) Y. Tanabe and S. Sugano, *J. Phys. Soc. Jpn.*, 1954, **9**, 766–779; (*c*) J. Oppenheim and J. Miller, *Tanabe-Sugano for*

Mathematica, 2019, available at: **https://github.com/JulesOpp/Tanabe-Sugano**, accessed 7 December 2021.

15 C. Wang, W. R. Kitzmann, F. Weigert, C. Förster, X. Wang, K. Heinze and U. Resch-Genger, *ChemPhotoChem*, 2022, e202100296.

16 (*a*) P. A. Scattergood, in *Organometallic Chemistry*, ed. N. J. Patmore and P. I. P. Elliott, Royal Society of Chemistry, Cambridge, 2020, vol. 43, pp. 1–34; (*b*) M. Dorn, N. R. East, C. Förster, W. R. Kitzmann, J. Moll, F. Reichenauer, T. Reuter, L. Stein and K. Heinze, in *Comprehensive Inorganic Chemistry III*, ed. J. Reedijk, Elsevier, San Diego, 2022.

17 S. Lenz, H. Bamberger, P. P. Hallmen, Y. Thiebes, S. Otto, K. Heinze and J. van Slageren, *Phys. Chem. Chem. Phys.*, 2019, **21**, 6976–6983.

18 A. B. P. Lever, *Inorganic electronic spectroscopy*, Elsevier, Amsterdam, 1st edn, 1968.

19 F. Reichenauer, C. Wang, C. Förster, P. Boden, N. Ugur, R. Báez-Cruz, J. Kalmbach, L. M. Carrella, E. Rentschler, C. Ramanan, G. Niedner-Schatteburg, M. Gerhards, M. Seitz, U. Resch-Genger and K. Heinze, *J. Am. Chem. Soc.*, 2021, **143**, 11843–11855.

20 S. Otto, J. P. Harris, K. Heinze and C. Reber, *Angew. Chem., Int. Ed.*, 2018, **57**, 11069–11073.

21 S. Otto, N. Scholz, T. Behnke, U. Resch-Genger and K. Heinze, *Chem. – Eur. J.*, 2017, **23**, 12131–12135.

22 P. Boden, P. Di Martino-Fumo, G. Niedner-Schatteburg, W. Seidel, K. Heinze and M. Gerhards, *Phys. Chem. Chem. Phys.*, 2021, **23**, 13808–13818.

23 R. A. Forman, G. J. Piermarini, J. D. Barnett and S. Block, *Science*, 1972, **176**, 284–285.

24 M. A. El-Sayed, *J. Chem. Phys.*, 1963, **38**, 2834–2838.

25 T. J. Penfold, E. Gindensperger, C. Daniel and C. M. Marian, *Chem. Rev.*, 2018, **118**, 6975–7025.

26 S. Otto, A. M. Nauth, E. Ermilov, N. Scholz, A. Friedrich, U. Resch-Genger, S. Lochbrunner, T. Opatz and K. Heinze, *ChemPhotoChem*, 2017, **1**, 344–349.

27 (*a*) K. Shizu and H. Kaji, *J. Phys. Chem. A*, 2021, **125**, 9000–9010; (*b*) S. Yabumoto, S. Sato and H. Hamaguchi, *Chem. Phys. Lett.*, 2005, **416**, 100–103.

28 K. Mack, A. Wünsche von Leupoldt, C. Förster, M. Ezhevskaya, D. Hinderberger, K. W. Klinkhammer and K. Heinze, *Inorg. Chem.*, 2012, **51**, 7851–7858.

29 C. Wang, S. Otto, M. Dorn, E. Kreidt, J. Lebon, L. Sršan, P. Di Martino-Fumo, M. Gerhards, U. Resch-Genger, M. Seitz and K. Heinze, *Angew. Chem., Int. Ed.*, 2018, **57**, 1112–1116.

30 U. Basu, S. Otto, K. Heinze and G. Gasser, *Eur. J. Inorg. Chem.*, 2019, 37–41.

31 E. Kreidt, C. Kruck and M. Seitz, in *Handbook on the physics and chemistry of rare earths. Including actinides*, ed. J.-C. G. Bünzli, V. K. Pecharsky, G.-Y. Adachi, K. A. Gschneidner and E. LeRoy, North-Holland, Amsterdam, Oxford, 2018, vol. 53, pp. 35–79.

32 O. Laporte and W. F. Meggers, *J. Opt. Soc. Am.*, 1925, **11**, 459.

33 S. Treiling, C. Wang, C. Förster, F. Reichenauer, J. Kalmbach, P. Boden, J. P. Harris, L. M. Carrella, E. Rentschler, U. Resch-Genger, C. Reber, M. Seitz, M. Gerhards and K. Heinze, *Angew. Chem., Int. Ed.*, 2019, **58**, 18075–18085.

34 J.-R. Jiménez, B. Doistau, C. M. Cruz, C. Besnard, J. M. Cuerva, A. G. Campaña and C. Piguet, *J. Am. Chem. Soc.*, 2019, **141**, 13244–13252.

35 J.-R. Jiménez, M. Poncet, S. Míguez-Lago, S. Grass, J. Lacour, C. Besnard, J. M. Cuerva, A. G. Campaña and C. Piguet, *Angew. Chem., Int. Ed.*, 2021, **60**, 10095–10102.

36 (*a*) J.-R. Jiménez, M. Poncet, B. Doistau, C. Besnard and C. Piguet, *Dalton Trans.*, 2020, **49**, 13528–13532; (*b*) S. Otto, C. Förster, C. Wang, U. Resch-Genger and K. Heinze, *Chem. – Eur. J.*, 2018, **24**, 12555–12563.

37 (*a*) N. Sinha, J.-R. Jiménez, B. Pfund, A. Prescimone, C. Piguet and O. S. Wenger, *Angew. Chem., Int. Ed.*, 2021, **60**, 23722–23728; (*b*) L. Stein, P. Boden, R. Naumann, C. Förster, G. Niedner Schatteburg and K. Heinze, *Chem. Commun.*, 2022, **58**, 3701–3704.

38 (*a*) M. Dorn, J. Kalmbach, P. Boden, A. Kruse, C. Dab, C. Reber, G. Niedner-Schatteburg, S. Lochbrunner, M. Gerhards, M. Seitz and K. Heinze, *Chem. Sci.*, 2021, **12**, 10780–10790; (*b*) M. Dorn, K. Mack, L. M. Carrella, E. Rentschler, C. Förster and K. Heinze, *Z. Anorg. Allg. Chem.*, 2018, **644**, 706–712; (*c*) J. P. Zobel, T. Knoll and L. González, *Chem. Sci.*, 2021, **12**, 10791–10801; (*d*) M. S. Fataftah, S. L. Bayliss, D. W. Laorenza, X. Wang, B. T. Phelan, C. B. Wilson, P. J. Mintun, B. D. Kovos, M. R. Wasielewski, S. Han, M. S. Sherwin, D. D. Awschalom and D. E. Freedman, *J. Am. Chem. Soc.*, 2020, **142**, 20400–20408.

39 (*a*) J. Kalmbach, C. Wang, Y. You, C. Förster, H. Schubert, K. Heinze, U. Resch-Genger and M. Seitz, *Angew. Chem., Int. Ed.*, 2020, **59**, 18804–18808; (*b*) C. Wang, F. Reichenauer, W. R. Kitzmann, C. Kerzig, K. Heinze and U. Resch-Genger, *Angew. Chem., Int. Ed.*, 2022, **61**, e202202238.

40 (*a*) C. Dee, F. Zinna, W. R. Kitzmann, G. Pescitelli, K. Heinze, L. Di Bari and M. Seitz, *Chem. Commun.*, 2019, **55**, 13078–13081; (*b*) M. Poncet, A. Benchohra, J.-R. Jiménez and C. Piguet, *ChemPhotoChem*, 2021, **5**, 880–892.

41 C. Wang, S. Otto, M. Dorn, K. Heinze and U. Resch-Genger, *Anal. Chem.*, 2019, **91**, 2337–2344.